

# Direct Numerical Simulation of the Moist Stably Stratified Surface Layer: Turbulence and Fog Formation

Michael MacDonald\* · Marcin J. Kurowski · João Teixeira

Received: DD Month YEAR / Accepted: DD Month YEAR

**Abstract** We investigate the effects of condensation and liquid water loading on the stably stratified surface layer, with an eye towards understanding the influence of turbulent mixing on fog formation. Direct numerical simulations (DNS) of dry and moist open channel flows are conducted, where in both a constant cooling rate is applied at the ground to mimic long-wave radiative cooling. Depending on the cooling rate, it can lead to either turbulent (weakly stable) or laminar (very stable) flows. Compared to the completely dry case, the condensation of liquid water in the moist case enables slightly higher cooling rates to be achieved before leading to turbulence collapse. In the very stable cases, runaway cooling leads to the substantial condensation of liquid water close to the ground and fog (visibility less than 1 km) results over much of the domain. In the weakly stable cases, turbulent mixing narrowly yields visibilities of 1 km close to the ground over a similar time period. However, despite the idealized nature of the system, the present results suggest that turbulence impedes, although will not necessarily inhibit, fog formation. A possible mechanism for fog formation within turbulent flows is identified, wherein regions of increased liquid water content form within the low-speed streaks of the near-wall cycle. These streaks are energized in the moist cases due to reduced dissipation of turbulence kinetic energy compared to the dry case, although in both cases the streaks are less energetic and persistent than in neutrally stratified flow.

© 2019 California Institute of Technology. U.S. Government sponsorship acknowledged.

**Keywords** Direct numerical simulation · Fog formation · Stable surface layer

---

\*M. MacDonald

Jet Propulsion Laboratory, California Institute of Technology, Pasadena, CA, USA and Department of Mechanical Engineering, The University of Auckland, Auckland, New Zealand  
E-mail: michael.macdonald@auckland.ac.nz

M. J. Kurowski · J. Teixeira

Jet Propulsion Laboratory, California Institute of Technology, Pasadena, CA, USA

## 1 Introduction

Fog is an important meteorological phenomenon that can have wide-reaching influences on human lives, transportation, and the economy (Gultepe et al. 2007). In the case of radiation fog, it forms within the stably stratified atmospheric boundary layer (SBL), wherein sufficient surface cooling leads to the air reaching its saturation point. Typically, this cooling occurs during nocturnal clear-sky conditions due to longwave radiation. Fog is defined when the resulting suspension of water droplets reduces visibility to below 1 km, while visibilities above this threshold but below approximately 11 km are called mist (NOAA 2017). Despite the importance and several decades of extensive research on fog, accurate forecasts remain challenging (Steenefeld et al. 2015). This is in part due to a lack of understanding of some of the fundamental physical processes involved in fog formation and the early stages of its growth (Gultepe et al. 2007).

Taylor (1917) provided a simple thermodynamic analysis of fog formation using a Clausius–Clapeyron diagram, in which cooling, mixing, and moistening are the three principle processes involved. All three processes may occur simultaneously during fog formation, although mixing alone is often not significant enough to cause fog (Teixeira 1999). Moreover, the role of turbulence and mixing on fog formation has often received a range of interpretations (Gultepe et al. 2007). One hypothesis (e.g. Brown and Roach 1976; Roach et al. 1976) is that very low, or absent, winds are necessary for radiation fog to form, as otherwise the vertical mixing produced by turbulence draws drier, warmer air from aloft and prevents the air from reaching its saturation point. An alternative view (e.g. Rodhe 1962; Welch et al. 1986; Duynkerke 1999) is that turbulent mixing is essential, as it combines air-masses of different humidity and temperature such that saturation is achieved. Furthermore, both mechanisms might be responsible for fog formation depending on the specific conditions. Here, we use direct numerical simulations (DNS) of a moist, stably stratified surface layer undergoing cooling as an idealized system to study the fundamental mechanisms and relationship between turbulent mixing and fog formation.

Recently, large-eddy simulations (LES) of fog have had some success in simulating the main characteristics and qualitative behaviour of the fog life cycle in stably stratified environments (Nakanishi 2000; Porson et al. 2011; Bergot 2013). Further LES studies (Bergot 2016; Maronga and Bosveld 2017; Mazoyer et al. 2017) have attempted to quantify the effect of turbulence on fog formation and its life cycle. However, a core uncertainty here is the ability of LES to simulate stably stratified flows, especially when the ground cooling is sufficient to lead to partial or complete turbulence collapse. Ideally, LES resolves the largest, energy-containing eddies and uses a subgrid-scale (SGS) model to account for the dissipative actions of the smallest eddies. In stably stratified flows, however, the largest eddies become suppressed due to the effort of drawing up heavier (cooler) fluid from below and pulling down lighter (warmer) fluid from above. With increasing stability the largest energy-containing scales approach the grid size, potentially leading the SGS model to predict near-zero turbulent fluxes (Chung and Matheou 2014). Alternatively, some models artificially predict excessive mixing (de Roode et al. 2017). While there are SGS models that can account for the effects of buoyancy in the weakly stable regime (e.g. Lilly 1962; Dardorff 1980; Moeng 1984; Bou-Zeid et al. 2010; Chung and Matheou 2014), there are still challenges when turbulence collapse is considered.

Further complications are introduced to considering fog when the non-linear mixing processes during fog formation occur at small length scales. For example, the buoyancy length scale,  $L_b = w_{rms}/N$ , gives the level of suppression of vertical motions due to the stable stratification (Stull 1988), where  $w_{rms}$  is the root-mean-square (r.m.s.) vertical velocity

fluctuations and  $N$  is the buoyancy frequency. From the field observations of Price (2011), fog occurred with  $N \approx 0.08 \text{ s}^{-1}$  and the vertical velocity fluctuations were near zero with  $w_{rms} \lesssim 0.1 \text{ m s}^{-1}$ . This therefore leads to  $L_b \sim 1.2 \text{ m}$ . Similarly, the Ozmidov length,  $L_{Oz} = \sqrt{\epsilon/N^3}$ , gives the smallest scale influenced by buoyancy, where  $\epsilon$  is the turbulence dissipation. For typical values of  $\epsilon \sim 10^{-3} \text{ m}^2 \text{ s}^{-3}$  then  $L_{Oz}$  is of the same order as  $L_b$ . Recent high-resolution field observations have also noted substantial temperature gradients close to the ground during fog formation with  $N \approx 0.4 \text{ s}^{-1}$  (Izett et al. 2019), suggesting  $L_B$  and  $L_{Oz}$  may be even smaller. Ultimately, this implies that LES, with horizontal grid spacings of several metres and at best vertical resolutions of 1 m (e.g. Bergot 2013; Maronga and Bosveld 2017), may not properly resolve the small-scale mixing in fog formation. For this reason, we will use DNS of the moist SBL in the present study, which to our knowledge is the first time such a technique has been used to study an idealized representation of fog formation. DNS solves the Navier–Stokes equations, directly resolving the dissipative Kolmogorov length scale with no turbulence parametrization.

The structure of the dry SBL was described by Monin (1970) as follows. The overall boundary layer, of height  $\delta$ , is split into two regions, with the lowermost region termed the surface layer. Here, Coriolis effects can be neglected and the thickness of the surface layer,  $h$ , is on the order of tens of metres. The surface layer is further divided, wherein buoyancy forces can be neglected in the so-called dynamic sublayer, with thickness on the order of the Obukhov length,  $L$ . The buffer layer ( $z \ll L$ ) exists close to the ground and accounts for viscous effects in the case of a smooth surface, or roughness effects otherwise. Above the buffer layer, viscosity or roughness becomes irrelevant and the only remaining length scale is the distance to the ground,  $z$ . This yields the familiar logarithmic mean velocity profile, as in neutrally stratified wall-bounded turbulence. The flow remains turbulent so long as the ground cooling is sufficiently weak, such that  $L$  is large, in the so-called weakly stable regime (Mahrt 1999). However, under sufficiently strong ground cooling,  $L$  becomes small and turbulence can collapse completely. This results in a laminar flow with so-called runaway cooling (Van de Wiel et al. 2007), and is termed the very stable regime (Mahrt 1999).

The dry SBL has been simulated in a variety of configurations using DNS. The surface layer can be simulated using an open channel flow of height  $h$ , driven by a constant pressure gradient. Two alternative approaches are typically used, in which either a constant cooling flux is applied to the ground and the transient response is studied (e.g. Nieuwstadt 2005; Flores and Riley 2011), or a constant temperature difference is applied between the bottom and top boundaries yielding a statistically steady flow (e.g. García-Villalba and del Álamo 2011). The Coriolis force is neglected and low-level jets and other large-scale features of the SBL are not observed. Simulations of the Ekman layer under stable stratification, meanwhile, attempt to represent the full SBL and include the Coriolis force (Shah and Bou-Zeid 2014; Ansonge and Mellado 2014; Gohari and Sarkar 2017). While some differences between Ekman layers and open channel flows were reported in the outer-layer of the flow (where  $z \sim h$ ), Ansonge and Mellado (2014) and Flores and Riley (2018) explicitly compared the near-wall region (buffer and logarithmic layers) of the two flows. They showed that the logarithmic velocity profile and the turbulence kinetic energy (TKE) budget were comparable in this region, suggesting that the outer-layer does not have a significant influence on the near-wall flow.

While the Reynolds numbers of DNS are relatively low, appropriate non-dimensionalization of turbulent flows often exhibits Reynolds number similarity scaling. In particular, Ansonge and Mellado (2014) demonstrated that the velocity profiles, TKE budget, and intermittency factor do not vary significantly with Reynolds number in the neutrally stratified Ekman

layer. Furthermore, the stably stratified surface-layer simulations of Flores and Riley (2011) demonstrated that the time evolution of the total mass flux and density gradient at the ground were similar for different Reynolds numbers with matched cooling rates. Similar validation will be performed here, which will enable extrapolation and comparison of the results of the present study at relatively low Reynolds numbers to those found in the atmosphere.

In this paper we perform DNS of both dry and moist horizontally homogeneous open-channel flows, in which the flow is initialized from a dry turbulent neutrally stratified flow and a constant cooling flux is then applied to the ground. This represents the surface layer just after sunset undergoing radiative cooling (as in Nieuwstadt 2005), wherein the resulting condensation and small-scale turbulent mixing are studied in the context of fog formation. The numerical procedure and simulation set-up are described and validated in Sect. 2. Particular attention is given in Sect. 2.2 to how this system can be treated as an idealized representation of the early stages of fog formation. Results are presented in Sect. 3, including an analysis of the fog development (Sect. 3.2) and of the turbulence collapse in dry and moist flows (Sect. 3.3). Finally, conclusions are offered in Sect. 4.

## 2 Methodology

### 2.1 Governing Equations and Simulation Set-up

We simulate a horizontally homogeneous open-channel flow driven by a constant pressure gradient and an imposed ground-cooling flux. This represents the same set-up as Nieuwstadt (2005) and Flores and Riley (2011), although in addition we include moisture effects to study the influence of condensation of liquid water. The incompressible Navier–Stokes equations with Boussinesq approximation are solved in Cartesian coordinates, along with transport equations for temperature,  $T$ , and water vapour mixing ratio,  $q_v$ . A bulk approximation for the liquid water mixing ratio,  $q_l$  is used, yielding

$$\nabla \cdot \mathbf{u} = 0, \quad (1)$$

$$\frac{\partial \mathbf{u}}{\partial t} + \mathbf{u} \cdot \nabla \mathbf{u} = -\frac{1}{\rho} \nabla \pi + \nu \nabla^2 \mathbf{u} - \mathbf{i} \frac{1}{\rho} \frac{dP}{dx} + \mathbf{k} \mathcal{B}, \quad (2)$$

$$\frac{\partial T}{\partial t} + \mathbf{u} \cdot \nabla T = \frac{L_v}{c_p} C_d + \nu_T \nabla^2 T, \quad (3)$$

$$\frac{\partial q_v}{\partial t} + \mathbf{u} \cdot \nabla q_v = -C_d + \nu_v \nabla^2 q_v, \quad (4)$$

$$\frac{\partial q_l}{\partial t} + \mathbf{u} \cdot \nabla q_l = C_d + \nu_v \nabla^2 q_l, \quad (5)$$

where  $\mathbf{u} = (u, v, w)$  is velocity in the streamwise (or mean flow,  $x$ ), spanwise ( $y$ ) and vertical ( $z$ ) directions;  $\pi$  is the pressure perturbation;  $\rho$  is the constant air density;  $t$  is time;  $\mathbf{i}$  and  $\mathbf{k}$  are the unit vectors in the streamwise and vertical directions, respectively;  $dP/dx$  is the imposed constant streamwise pressure gradient that drives the flow;  $\nu$  is the constant molecular kinematic viscosity;  $\nu_T$  and  $\nu_v$  are the thermal and water vapour molecular diffusivities, which are constant and related to viscosity through the molecular Prandtl number,  $Pr_m = \nu/\nu_T = \nu/\nu_v = 0.71$ ; and  $C_d$  is the condensation rate, which maintains thermodynamic equilibrium with zero supersaturation (Grabowski and Smolarkiewicz 1990).  $\mathcal{B}$  is the buoyancy, defined as

$$\mathcal{B} \equiv g \left[ \frac{T - T_0}{T_0} + \epsilon(q_v - q_{v0}) - q_l \right], \quad (6)$$

where  $g = 9.81 \text{ m s}^{-2}$ ,  $T_0$  and  $q_{v0}$  are the reference temperature and water vapour mixing ratio, respectively, and  $\epsilon + 1 = R_v/R_d \approx 1.61$  is ratio of the gas constants for water vapour and dry air. The latent heat of condensation is  $L_v = 2.5 \times 10^6 \text{ J kg}^{-1}$  and specific heat at constant pressure is  $c_p = 1005 \text{ J kg}^{-1} \text{ K}^{-1}$ .

The governing equations above are solved using the finite volume, non-hydrostatic anelastic model EULAG, broadly documented in the literature (Grabowski and Smolarkiewicz 1990; Smolarkiewicz and Margolin 1997, 1998; Grabowski and Smolarkiewicz 2002; Andrejczuk et al. 2004; Kurowski et al. 2014), with a review in Prusa et al. (2008). The second-order accurate Eulerian (flux form) mode of EULAG is used in the present work. The present bulk approximation for  $q_l$ , along with a more detailed microphysical scheme that models supersaturation and the size dependence of multiple cloud droplets on sedimentation and evaporation, have previously been tested with EULAG in Andrejczuk et al. (2004, 2006, 2009). There, the authors performed DNS of cloud filaments embedded within decaying turbulence in a triply periodic domain. They only observed moderate differences between the bulk and detailed microphysics schemes, indicating that the bulk liquid water scheme used for the present DNS of the moist SBL is likely adequate. A similar bulk scheme has also been used in DNS studies of stratocumulus cloud tops (Mellado 2010; Mellado et al. 2010, 2014) as well as in the LES study of radiation fog in Nakanishi (2000).

Simulations are conducted in an open channel, consisting of periodic boundary conditions in the lateral directions. The lower wall (or ground, subscript  $g$ ) at  $z = 0$  consists of no-slip ( $u = v = 0$ ) and impermeability ( $w = 0$ ) conditions with an imposed constant (cooling) heat flux ( $H_g < 0$ , described in Sect. 2.3) and zero total water flux ( $d(q_v + q_l)/dz = 0$ ). The upper boundary at  $z = h$  is a free-slip ( $du/dz = dv/dz = 0$ ) impermeable wall with zero total water flux and constant temperature ( $T - T_0 = 0$ ). Both dry (only Eqs. 1–3, with no water vapour and liquid water) and moist (Eqs. 1–5) flows are simulated with the same imposed ground heat flux, so that the effects of liquid water can be analyzed independently of the ground cooling.

A snapshot from the turbulent quasi-stationary neutrally stratified dry case is used to initialize the flow, after which the ground cooling flux is applied. The initial thermodynamic state is set to air at standard atmospheric pressure (1013 hPa) with density  $\rho = 1.265 \text{ kg m}^{-3}$  and viscosity  $\nu = 1.38 \times 10^{-5} \text{ m}^2 \text{ s}^{-1}$ . The temperature is initialized as  $T_0 = 279.15 \text{ K}$  everywhere, although a case with higher temperature of  $T_0 = 285.15 \text{ K}$  is also simulated and shows little difference (see Appendix 2). The initial relative humidity is set to  $RH_0 = 99.9\%$  throughout the domain, corresponding to  $q_{v0} \approx 6.24 \text{ g kg}^{-1}$ . This large value of  $RH_0$  is used as lower values are computationally inefficient at reaching saturation, and is discussed further in Sect. 2.2. The air is initialized with no liquid water,  $q_{l0} = 0$ .

In subsequent sections, temporal averaging is denoted with an over bar,  $\bar{\cdot}$ , while spatial averaging in the horizontal plane is denoted by angled brackets,  $\langle \cdot \rangle$ . Velocity fluctuations are defined based on the difference between the instantaneous, spatially dependent velocity and its spatially averaged velocity at a given vertical location and time,  $u'(x, y, z, t) = \langle u \rangle(z, t) - u(x, y, z, t)$ . Root-mean-square (r.m.s.) velocity fluctuations are then defined as  $u'_{rms}(z, t) = \langle u'^2 \rangle^{1/2}$ .

## 2.2 Applicability to Fog Formation

The simulation set-up detailed above enables us to study the influence of moisture on the stable surface layer. More generally however, this system can also be treated as an idealized representation of fog formation within the atmosphere. Here, we are isolating just the

influence of the small-scale turbulent mixing on fog formation over the relatively short turbulence time scales. As such we deliberately neglect other competing processes; some of the key assumptions and limitations of this idealized system in the context of fog formation are discussed below.

The present bulk liquid water approximation assumes that the disperse liquid phase,  $q_l$ , can be modelled as a continuum. As discussed in Mellado et al. (2010), this condition is generally not met at the tops of stratocumulus clouds, as the cloud droplets of diameter  $d \approx 10 \mu\text{m}$  and number density  $N_d = 1000 \text{ cm}^{-3}$  are too sparse within a volume of the order of the Kolmogorov length scale,  $l_\eta = 1 \text{ mm}$  (i.e., that used in DNS). A similar problem exists for fog, as the Kolmogorov length scale is of the same order, however the droplets are even sparser with  $N_d \approx 10\text{--}100 \text{ cm}^{-3}$  and diameter  $1\text{--}10 \mu\text{m}$  (Roach et al. 1976; Price 2011). In addition, we assume the liquid water diffusivity is equal to that of water vapour. We also assume thermodynamic equilibrium, wherein phase changes occur instantaneously to maintain saturation through the condensation rate  $C_d$ . These assumptions may not hold for fog formation and, furthermore, predicting their impact on the present results is not trivial. However, they form useful approximations which are commonly employed in DNS studies of cloudy boundaries, notably stratocumulus cloud tops (e.g., Mellado 2010; Mellado et al. 2014; de Lozar and Mellado 2015, 2017). As this is a dynamically similar problem to fog, which involves the mixing of saturated and unsaturated air within a stably stratified environment, we employ the same assumptions in the present study.

Direct numerical simulation of the top of stratocumulus clouds have also shown radiation and droplet sedimentation to be an important process governing the mixing of clear and cloudy air (de Lozar and Mellado 2015, 2017). While stratocumulus cloud tops are a dynamically similar problem, fog in its early formation stages is unlikely to be optically thick enough for radiation effects to be significant. It is only once the fog is a few metres thick (i.e. on the scale of the present domain) that radiation is thought to become important (Oliver et al. 1978), wherein the radiative cooling enhances fog growth. In the present simulations the liquid water mixing ratio is typically less than  $0.01 \text{ g kg}^{-1}$  and so we neglect radiation effects. For simplicity, we also neglect droplet sedimentation effects, similar to the DNS study of stratocumulus tops by Mellado et al. (2014), which only considered shear and evaporative cooling in isolation. Moreover, it has been suggested that droplet sedimentation and radiative cooling are strongly dependent on one another, based on simple one-dimensional fog models (Brown and Roach 1976; Bott et al. 1990) and studies of individual cloud or fog droplets (Roach 1976; Barkstrom 1978). This suggests that both processes would need to be modelled together.

The present simulations neglect any moisture flux through the ground and more broadly there are no soil-vegetation effects, which are important in fog formation (Gultepe et al. 2007). Additional simulations were run with an imposed downwards moisture flux, representing dew deposition and hygroscopic absorption. The magnitude of this moisture flux was approximately equivalent to  $20 \text{ g m}^{-2} \text{ hr}^{-1}$ , similar to that observed during one of the fog formation cases in the field study of Price and Clark (2014). However, in the present system this caused a significant drying influence and completely inhibited all condensation. Similarly, reducing the initial relative humidity to a uniform value of 99.5% (with zero moisture flux boundaries) to enable more realistic water vapour gradients to develop also inhibited condensation. These two results are presumably due to a lack of moisture entering the system, so that the ground cooling alone is then insufficient to lead to condensation within reasonable simulation times. The present simulations therefore use the simpler configuration of zero moisture flux and a high initial relative humidity, rather than attempting to specify the complex moisture fluxes that occur with the ground or the atmosphere (either

due to horizontal heterogeneity or from higher up in the boundary layer) at such small scales necessary for DNS.

### 2.3 Scaling Variables

The characteristic velocity scale within the surface layer is the friction velocity (Monin 1970). Following Flores and Riley (2011), we distinguish between the (constant) friction velocity obtained from the imposed driving pressure gradient,  $U_*^2 = -(h/\rho)dP/dx$ , and from the spatially averaged wall-shear stress,  $u_\tau^2(t) = \tau_w/\rho = \nu d\langle u \rangle/dz|_g$ . The latter can vary with time due to accelerations in the bulk velocity,  $u_b(t) = (1/h)\int_0^h \langle u \rangle dz$ , caused by the ground cooling. For the neutrally stratified dry cases, a statistically steady state is obtained such that the bulk velocity is approximately constant over time and  $\overline{u_\tau} = U_*$ . As such,  $U_*$  can be regarded as the reference friction velocity of the neutrally stratified case, which is matched for all simulations with the same  $Re_*$ .

The characteristic temperature, water vapour, and length scales will be related to  $H_g < 0$ , the imposed (cooling) heat flux that is applied to the ground at  $t = 0$ . This heat flux is matched between respective dry and moist cases. In response, sensible and, when saturation occurs, latent heat fluxes will be directed toward the surface. These fluxes, when horizontally averaged, are given as (Monin 1970)

$$H_s(z, t) = \rho c_p \left( \nu_T \frac{d\langle T \rangle}{dz} - \langle w'T' \rangle \right), \quad (7)$$

$$H_l(z, t) = \rho L_v \left( \nu_v \frac{d\langle q_v \rangle}{dz} - \langle w'q'_v \rangle \right). \quad (8)$$

In meteorology, the conduction (gradient) terms of temperature and water vapour are often ignored as they are considered negligible relative to the turbulent fluxes. However, as we are resolving the viscous sublayer with impermeability constraint in the present DNS,  $w(z=0) = 0$ , the gradient terms become significant at the ground (Businger 1982) whereas the turbulent fluxes vanish. As such, the imposed ground heat flux can be seen to prescribe the temperature and water vapour gradients,

$$H_g = H_s(0, t) + H_l(0, t) \quad (9)$$

$$= \rho c_p \nu_T \left. \frac{d\langle T \rangle}{dz} \right|_g + \rho L_v \nu_v \left. \frac{d\langle q_v \rangle}{dz} \right|_g. \quad (10)$$

In the SBL, the characteristic length scale is taken to be the Obukhov length,  $L$ , as discussed in Sect. 1. This can be interpreted as the height at which buoyancy effects dominate over mechanical (shear) production of turbulence kinetic energy (Stull 1988). The Obukhov length is a function of the ground cooling and is defined as

$$L = -\frac{U_*^3/\kappa}{(g/T_0)H_g/(\rho c_p)}, \quad (11)$$

where  $\kappa = 0.41$  is the von Kármán constant, included for historical reasons. In LES models and field studies the heat flux at the ground is often taken to be the vertical turbulent heat flux,  $\langle w'T' \rangle$ , at the lowest level. However, as mentioned above, these fluxes vanish at the ground so that Eq. 10 is used to define  $H_g$ . The ratio between the surface layer height (or channel half height) and the (imposed) Obukhov length,  $h/L$ , is often reported in stably

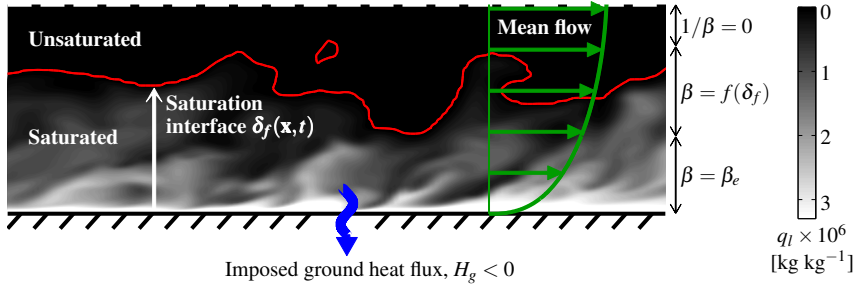


**Fig. 1** Cross-section of the streamwise–vertical plane showing an instantaneous snapshot of the liquid water mixing ratio for case 395M06. The saturation interface,  $\delta_f$ , where  $q_l > 0$ , varies in space and grows in time as the ground continues to be cooled through the imposed heat flux,  $H_g$ . Variations in the Bowen ratio,  $\beta$ , are shown on the right

stratified DNS studies; when  $h/L \lesssim 1$  the cooling is relatively weak while  $h/L \gtrsim 1$  corresponds to stronger cooling. Note, however, that the ratio  $h/L$  is not a suitable measure for turbulence collapse as it is Reynolds number dependent (Nieuwstadt 2005; Flores and Riley 2011). In addition, there are two characteristic length scales in neutrally stratified wall turbulence, namely  $h$ , the outer-layer or large-scale length scale and  $\nu/U_*$ , the inner-layer, near-ground or viscous length scale. Both of these will be used here; superscript  $+$  indicates non-dimensionalization on  $\nu$  and  $U_*$ . For example,  $z^+ = zU_*/\nu$  is the vertical position non-dimensionalized on the viscous length scale.

The horizontally averaged Bowen ratio,  $\beta(z, t) = H_s/H_l$ , gives the ratio between the sensible and latent heat fluxes. At a given vertical height,  $z$ , there could exist regions of unsaturated air ( $H_l = 0$ ) alongside regions of non-zero liquid water mixing ratios ( $H_l > 0$ ). Hence, as with the heat fluxes, the Bowen ratio is a function of both vertical position and time. When a vertical level is completely saturated,  $\beta$  will tend towards the equilibrium Bowen ratio  $\beta_e$  due to the use of the bulk condensation model that maintains thermodynamic equilibrium (Sect. 2.1). Based on the present thermodynamic state, this can be estimated as  $\beta_e = (c_p/L_v)/(\partial q_{sat}/\partial T) \approx 0.92$  (Stull 1988). Meanwhile, in the dry cases and moist cases where the air is completely unsaturated at a given  $z$ , there is no latent heat flux and  $1/\beta = 0$  (cf. Fig. 1)

The instantaneous friction temperature and water vapour can now be defined as

$$T_\tau(z, t) = -\frac{H_s}{\rho c_p u_\tau} = -\frac{H_g/(1 + 1/\beta)}{\rho c_p u_\tau}, \quad (12)$$

$$q_\tau(z, t) = -\frac{H_l}{\rho L_v u_\tau} = -\frac{H_g/(\beta + 1)}{\rho L_v u_\tau}. \quad (13)$$

Crucially, these can not be known a priori as they depend on the evolution of  $\beta(z, t)$  (or the saturation interface  $\delta_f$ ) and instantaneous wall-shear stress through  $u_\tau(t)$ . These quantities vary with height and time, which can be interpreted using the internal boundary layer framework (Elliott 1958; Panofsky and Townsend 1964). For example, after a step change in roughness, the flow above the newly formed internal boundary layer (IBL) still depends on the friction velocity of the original surface upstream, while that within the IBL scales with the friction velocity of the new surface. In the present moist simulations, the flow at the top of the domain when unsaturated would depend on  $T_\tau$  defined with  $1/\beta = 0$ , as the information regarding the saturated condition has not yet reached this height. The flow close to the ground, where liquid water has condensed, would meanwhile depend on  $T_\tau$  defined



**Table 1** Details of the simulations performed.  $N_{runs}$  is the number of runs using unique initialization snapshots from the dry, neutrally stratified case

ID	$Re_\star$	$N_{runs}$	$h/L$	Final state
395D00	395	1	0	Turbulent
395D041	395	1	0.41	Turbulent
395M041	395	1	0.41	Turbulent
395D06	395	3	0.6	Turb., Lam.
395M06	395	3	0.6	Turbulent
395D07	395	1	0.7	Laminar
395M07	395	1	0.7	Laminar
395D205	395	1	2.05	Laminar
395M205	395	1	2.05	Laminar
590D06	590	1	0.6	Turbulent
590M06	590	1	0.6	Turbulent
590D085	590	1	0.85	Turbulent
590M085	590	1	0.85	Turbulent

with  $\beta \rightarrow \beta_e \approx 0.92$ . Note that rather than growing spatially, as in conventional IBL depictions, the saturation interface grows temporally due to the periodic boundary conditions in the streamwise direction, which imposes horizontal homogeneity (Mellado 2012; Kozul et al. 2016). We can define a constant friction temperature and water vapour, analogous to the  $U_\star$  friction velocity, using the equilibrium Bowen ratio,

$$T_\star = -\frac{H_{s,g}}{\rho c_p U_\star} = -\frac{H_g/(1+1/\beta_e)}{\rho c_p U_\star}, \quad (14)$$

$$q_\star = -\frac{H_{l,g}}{\rho L_v U_\star} = -\frac{H_g/(\beta_e + 1)}{\rho L_v U_\star}; \quad (15)$$

however this assumes fully saturated conditions across the entire domain. The value of  $T_\tau$  and  $q_\tau$  would therefore converge to  $T_\star$  and  $q_\star$  (for all  $z$ ), although only when  $t$  becomes sufficiently large.

## 2.4 Description of Cases

Table 1 details the different simulations conducted. We independently vary the friction Reynolds number,  $Re_\star = U_\star h/\nu$  and Obukhov length,  $L$ . Cases are referred to with an ID of their friction Reynolds number, whether the case is dry or moist, and the ratio between channel half height and Obukhov length. For example, case 395M06 is a moist case performed at  $Re_\star = 395$  with  $h/L = 0.6$ . A constant grid-spacing is used in the horizontal directions, with  $\Delta x^+ = \Delta x U_\star/\nu \approx 9.7$  and  $\Delta y^+ \approx 4.8$ . A hyperbolic tangent grid stretching is used in the vertical direction (Moin and Kim 1982), resulting in grid spacings at the ground and channel centre of  $\Delta z|_{z=0}^+ \approx 0.35$  and  $\Delta z|_{z=h}^+ \approx 7.0$ , respectively. These grid spacings are in good agreement with those used in previous stably stratified DNS studies (e.g. Flores and Riley 2011; García-Villalba and del Álamo 2011; Gohari and Sarkar 2017). The DNS studies of Anson and Mellado (2014) and Shah and Bou-Zeid (2014), meanwhile, had matched streamwise and spanwise grid spacings with  $\Delta x^+ = \Delta y^+ \gtrsim 4$  and thus had a finer streamwise grid spacing than the present case. However, if we assume that viscous dissipation equals the production of total turbulence kinetic energy,  $\epsilon = -u_b dP/dx$  (e.g. Nieuwstadt 2005), then the present grid spacings can be related to the Kolmogorov

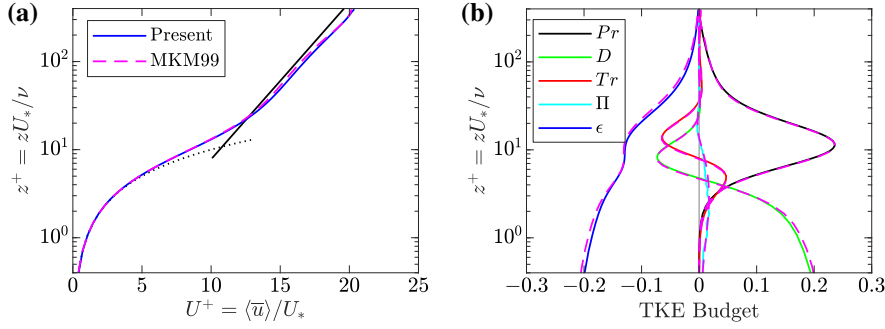


**Fig. 2** Profiles of (a) velocity and (b) TKE budget for the present dry neutrally stratified case (solid lines) and the DNS data of Moser et al. (1999) (magenta dashed lines) at  $Re_* = hU_*/\nu = 395$ . In (a), the dotted black line shows the viscous sublayer velocity,  $U^+ = z^+$ , while the solid black line shows the logarithmic velocity profile,  $U^+ = (1/0.41) \log(z^+) + 5.2$ . The TKE budget terms in (b) are given in Eq. 16 and normalized on  $U_*^4/\nu$ ; note that the buoyancy production,  $B$ , is zero

length,  $\eta = (\nu^3/\epsilon)^{1/4}$ , as  $\Delta x = 4.0\eta$ ,  $\Delta y = 2.0\eta$ ,  $\Delta z|_{z=0} = 0.15\eta$  and  $\Delta z|_{z=h} = 2.9\eta$ . They are therefore all  $O(\eta)$ , in agreement with the grid-spacing recommendations for conventional DNS (Moin and Mahesh 1998). For the cases with  $Re_* = 395$  and  $h/L = 0.6$ , multiple runs are performed in which unique initialization snapshots from the dry neutrally stratified case are used for both dry and moist cases (395D06 and 395M06). The computational domain size is set to  $L_x \times L_y = 2\pi h \times \pi h$ , which is commonly employed for neutrally stratified dry simulations (Lozano-Durán and Jiménez 2014; Munters et al. 2016). The effect of the domain size is investigated in Appendix 1, showing that while the domain is relatively small for stably stratified flows, it should not alter the conclusions of this paper. The present simulations use  $256 \times 256 \times 128$  grid points for the  $Re_* = 395$  cases and  $384 \times 384 \times 192$  grid points for the  $Re_* = 590$  cases to obtain the grid spacings mentioned above.

## 2.5 Validation of EULAG

The neutrally stratified dry case, 395D00, is first validated with the DNS data of Moser et al. (1999, herein MKM99) at a friction Reynolds number  $Re_* = hU_*/\nu = 395$ . This case obtains a statistically steady state independent of the initial conditions, identified by a linear profile of the total stress profile,  $-\langle u'w' \rangle + \nu d\langle \bar{u} \rangle/dz$  (Kim et al. 1987). The flow is then temporally averaged over  $tU_*/h \approx 20$  large-eddy turnover times. Figure 2 shows the mean velocity profile and (resolved) TKE budget for the present data from EULAG, along with the DNS data of MKM99. Good agreement is observed between the two datasets, indicating that EULAG can be readily used for surface-layer simulations. The budget for the horizontally

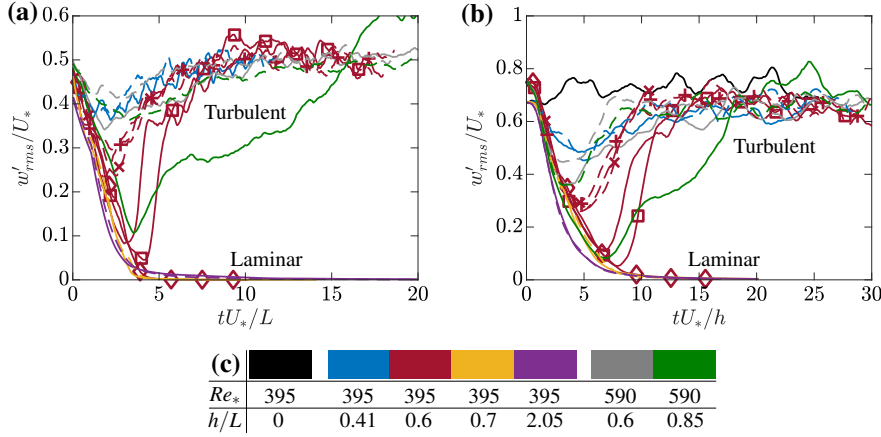


**Fig. 3** Time series of the r.m.s. vertical velocity fluctuations at (a)  $z^+ \approx 15$ , and at (b)  $z/h \approx 2/3$ . Line colours defined in (c), corresponding to cases listed in Table 1. Solid lines represent dry cases, while dashed lines represent moist cases. Additional runs for  $Re_* = 395$ ,  $h/L = 0.6$  with unique initialization snapshots are indicated with symbols;  $\diamond$  and  $\times$  are dry and moist cases, respectively, for the same snapshot; likewise  $\square$  and  $+$  for the other snapshot. Note the time normalization is different in (a) and (b) following Flores and Riley (2011); as such the neutrally stratified case ( $L = \infty$ ) is not plotted in (a)

averaged TKE,  $e = \langle u'_i u'_i \rangle / 2$ , is shown in Fig. 2b, where the terms correspond to

$$\frac{\partial e}{\partial t} = \underbrace{-\langle u'w' \rangle \frac{\partial \langle u \rangle}{\partial z}}_{Pr} + \underbrace{\nu \frac{\partial^2 e}{\partial z^2}}_D + \underbrace{-\frac{\partial \langle ew' \rangle}{\partial z}}_{Tr} + \underbrace{-\frac{1}{\rho} \frac{\partial \langle \pi'w' \rangle}{\partial z}}_II + \underbrace{\frac{g}{T_0} \langle w'T' \rangle}_B - \underbrace{\nu \left\langle \frac{\partial u'_i}{\partial x_j} \frac{\partial u'_i}{\partial x_j} \right\rangle}_\epsilon, \quad (16)$$

where  $Pr$  is the mechanical (or shear) production,  $D$  the viscous diffusion,  $Tr$  the turbulent transport,  $II$  the pressure correlation,  $B$  the buoyant production and  $\epsilon$  the (pseudo-)dissipation. The left hand side, referred to as the tendency or residual, is zero for this neutrally stratified flow due to it achieving a statistically steady state. Conventional summation notation is used for repeated subscripts of  $i$  and  $j$ . The Reynolds stress terms,  $\langle u'_i u'_j \rangle$  (not shown) were also in good agreement with MKM99, although the vertical Reynolds stress,  $\langle w'w' \rangle$  went to zero at  $z = h$  due to the use of the slip, impermeable boundary condition. This reduction of  $\langle w'w' \rangle$  began at approximately  $z/h \approx 0.8$  in agreement with other open channel simulations (e.g. MacDonald et al. 2017).

### 3 Results

#### 3.1 Temporal Evolution of Turbulent Fluctuations

The imposed ground cooling can either lead to complete turbulence collapse, resulting in laminar flow (very stable regime), or maintenance of the turbulent flow (weakly stable regime). To highlight these two regimes, Fig. 3 shows the time series of the r.m.s. of the

vertical velocity fluctuations at two different heights,  $z^+ \approx 15 \approx 0.04h^+$  (i.e. close to the ground, within the buffer layer) and  $z/h \approx 2/3$ . A moving average filter of size  $1h/U_*$  is applied to the present time series for clarity. Figure 3 matches Fig. 3 of Flores and Riley (2011) and, as discussed in Flores and Riley (2011), the temporal adjustment to the imposed cooling scales with  $L/U_*$  in the buffer layer (Fig. 3a), while in the outer layer (Fig. 3b) it scales with  $h/U_*$ . The neutrally stratified case is therefore not shown in Fig. 3a as  $L = \infty$ .

In general, the cooling causes a reduction in the vertical velocity fluctuations within the first 5–10 large-eddy turnover times. In the weakly stable cases the turbulence then recovers to magnitudes close to the neutrally stratified case, while for very stable cases the turbulence collapses and the fluctuations tend to zero. As will be seen later, in the moist cases (dashed lines) saturation begins at the ground almost immediately. The associated latent heat release and buoyancy effects due to condensation appear to cause increased mixing in the moist case, leading to the turbulent fluctuations remaining larger compared to the dry cases (solid lines) at matched  $h/L$ . This is especially evident when the flow is close to laminarization. In particular, for cases 395D06 and 395M06 three different initialization snapshots were run with cooling of  $h/L = 0.6$ , wherein the cooling is sufficient to lead to complete turbulence collapse for one of the dry runs (red solid line with diamond symbols) but not the other two. Meanwhile, all three moist runs remained weakly stable and maintained turbulence.

The exact critical value of  $h/L$  that leads to turbulence collapse has been recognized as being Reynolds number dependent, with Nieuwstadt (2005) observing a critical value of  $h/L = 0.51$  for  $Re_* \approx 360$ , while Flores and Riley (2011) observed the critical value to be  $h/L = 0.82$  for  $Re_* \approx 560$ . The present values of  $h/L \approx 0.6$  for  $Re_* \approx 395$  and  $h/L \gtrsim 0.85$  for  $Re_* \approx 590$  for the dry cases therefore agree with this trend. Due to the Reynolds number dependence in  $h/L$ , Flores and Riley (2011) suggested that  $L_\tau u_\tau / \nu$  is a better measure for the critical cooling level, where  $L_\tau$  is the Obukhov length defined using the instantaneous wall-shear stress  $u_\tau$  (as opposed to the constant driving  $U_*$ , as in Eq. 11). The two dry runs of 395D06 which sustained turbulent flow were observed to have a minimum  $L_\tau u_\tau / \nu \approx 95$ , while the other initialization snapshot, which led to turbulence collapse, had  $L_\tau u_\tau / \nu \leq 75$ . This agrees with the observation in Flores and Riley (2011) that turbulence collapses when  $L_\tau u_\tau / \nu \lesssim 100$ , due to insufficient scale separation between the length scale of turbulent production in the buffer region (approximately  $100\nu/u_\tau$ ) and the buoyancy length scale ( $L_\tau$ ). The moist cases with  $Re_* = 395$  and  $h/L = 0.6$  had a minimum  $L_\tau u_\tau / \nu \approx 225$  for all three initialization snapshots, although for  $h/L = 0.7$  it was  $L_\tau u_\tau / \nu \approx 70$  and led to turbulence collapse. Compared to the dry case with critical  $h/L = 0.6$ , the production of liquid water enables a slightly larger cooling rate to be achieved before leading to turbulence collapse, with critical  $h/L$  in the range 0.6–0.7.

Note that, as discussed in Flores and Riley (2011) and García-Villalba and del Álamo (2011), the asymptotic laminar friction Richardson number,  $Ri_{\tau,l} = (2/\kappa)(h/L)Re_*Pr_m$  for all the present cases is less than the linear stability limit (Gage and Reid 1968). Therefore we would expect the cases with laminar flow to eventually recover a turbulent state given enough time. Also, purely laminar flow across the entire surface layer is unlikely to occur in the real atmosphere due to turbulence generated by large-scale structures that are not captured in the present idealized system, such as low-level jets and the breaking of gravity waves (Flores and Riley 2011).

The effects of the relatively small computational domain size are evident in the dry higher Reynolds number cases (particularly 590D085, green solid line), where it takes longer to return to the statistically steady turbulent state. This is due to the existence of ‘locked’ turbulent structures (Flores and Riley 2011; García-Villalba and del Álamo 2011), where adjacent turbulent and laminar patches become locked in place as a result of the periodic

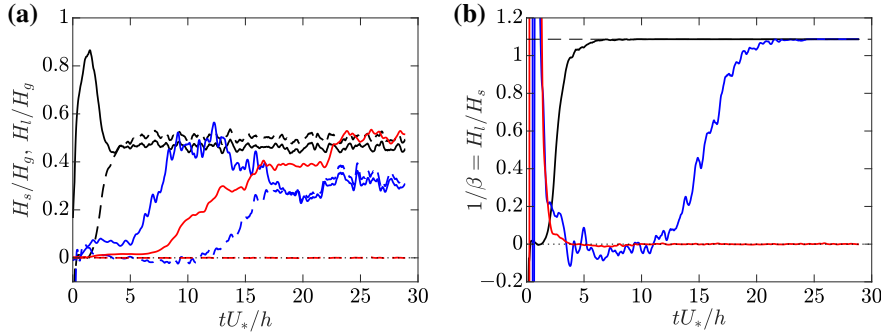


**Fig. 4** Time series of (a) sensible (solid) and latent (dashed) heat fluxes normalized on the imposed ground heat flux,  $H_g$ , and (b) inverse of the Bowen ratio,  $1/\beta = H_l/H_s$ . These are shown at  $z^+ \approx 15$  (black),  $z/h = 2/3$  (blue), and  $z = h$  (red) for case 395M06. Equilibrium Bowen ratio  $1/\beta_e \approx 1.09$  shown by horizontal dashed line in (b)

boundary conditions (see also Appendix 1). The moist case, meanwhile, does not exhibit this behaviour for the same cooling rate. This is possibly due to the latent heat released during condensation, which would enhance mixing due to buoyancy production. Moreover, a positive feedback system exists wherein any tendency toward a laminar state with reduced mixing would result in enhanced, or runaway, cooling (Van de Wiel et al. 2007). This would therefore promote condensation-induced mixing and thus avoid the spatially locked laminar patches associated with turbulence collapse. Note that this effect may be sensitive to the domain size (García-Villalba and del Álamo 2011; Ansonge and Mellado 2014) and would require further investigation.

Before analyzing variations in the r.m.s. of temperature fluctuations, Fig. 4a shows how the sensible and latent heat fluxes transported by the fluid change over time for case 395M06. Close to the ground, at  $z^+ \approx 15$ , the sensible heat flux (black solid line) initially increases rapidly due to the imposed ground heat flux. However, soon thereafter the temperature reaches saturation point and liquid water condenses, resulting in an increase in the latent heat flux (black dashed line) and decrease in the sensible heat flux. Within five large-eddy turnover times, the latent and sensible heat fluxes reach a statistically steady state and the inverse of the Bowen ratio (Fig. 4b) is exactly equal to its equilibrium value (horizontal dashed line). This does not vary with time due to the use of the bulk condensation model, which maintains equilibrium conditions. A similar effect occurs for the heat fluxes higher up at  $z/h = 2/3$  (blue lines), although this is delayed as the interface between saturated and unsaturated air requires time to grow upwards (see sketch in Fig. 1). Note that the sum of  $H_s$  and  $H_l$  at this height does not equal  $H_g$  as the flow has not achieved a true statistically steady state; this would only occur when the heat flux at the top of the domain balances the imposed ground heat flux. No significant amount of liquid water reaches the top of the domain ( $z = h$ , red line) so the latent heat flux and Bowen ratio remains essentially zero.

The r.m.s. temperature fluctuations (Fig. 5) are initially zero before increasing with time, as  $T$  is uniformly set to  $T_0$  at  $t = 0$ . The temperature in Fig. 5 is normalized on the instantaneous, vertically dependent friction temperature  $T_\tau(z, t)$  from Eq. 12. This choice of normalization results in good agreement between dry and moist turbulent cases with different cooling rates, as well as for the different Reynolds number cases. Figure 5a shows the r.m.s. temperature fluctuations close to the ground at  $z^+ \approx 15$ . The large peaks around  $tU_* / h \approx 10$  for the dry cases 395D06 and 590D085 (solid red and green lines, Fig. 5a)

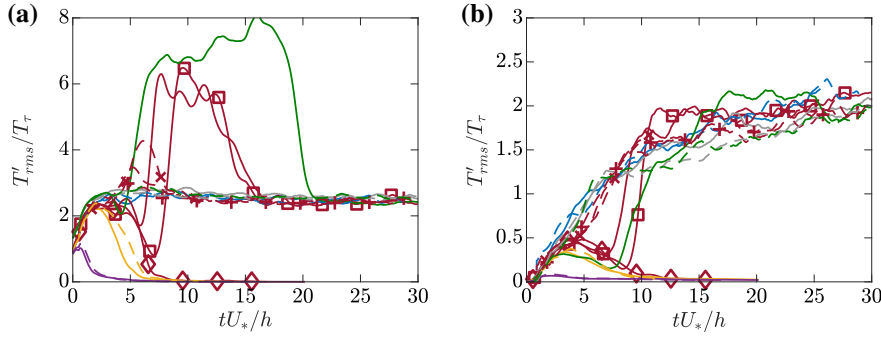


**Fig. 5** Time series of r.m.s. temperature fluctuations at (a)  $z^+ \approx 15$ , and at (b)  $z/h = 2/3$ . Line styles same as Fig. 3. Temperature normalized on  $T_\tau(z, t)$  (Eq. 12), defined on instantaneous  $\beta$  and  $u_\tau$

are due to spatial intermittency of turbulent/laminar patches, which are locked in place due to the periodic boundary conditions (Flores and Riley 2011; García-Villalba and del Álamo 2011).

Figure 5b shows the temperature fluctuations in the outer layer at  $z/h = 2/3$ . As discussed with Fig. 4, the downwards heat flux has not reached a statistically steady state and so we see  $T'_{rms}$  increases with time for both the dry and moist cases. Critically, by normalizing on the friction temperature  $T_\tau$  defined with varying Bowen ratio  $\beta$ , we see that the temperature fluctuations in the moist case do not vary when the saturation interface reaches this level. The fluctuations remain similar to the dry cases, despite the moist case having both intermittent unsaturated and saturated regions as the saturation interface reaches this level (which occurs around  $tU_*/h \approx 10$ – $20$  for cases 395M041 and 395M06). Moreover, once the air at  $z/h = 2/3$  becomes completely saturated after approximately 20 large-eddy turnover times the moist temperature fluctuations still remain similar to the dry cases. This suggests that these fluctuations within the saturated air are similar to those in the dry air when appropriately normalized.

### 3.2 Fog Development

Before analyzing the liquid water mixing ratio,  $q_l$ , we note that values of  $q_l$  can be converted to visibility values according to the empirical relationship from Kunkel (1984),

$$VIS(z, t) = -\frac{\log(0.02)}{144.7(\rho(q_l))^{0.88}}, \quad (17)$$

where  $VIS$  is measured in metres. The visibility values are typically much larger than the surface layer height and therefore domain size ( $VIS \gg h$ ), and this empirical relationship is unlikely to be entirely appropriate for the present idealized system. As such, we only use  $VIS$  for providing simple, qualitative descriptions in the context of fog. For reference, values of  $q_l = 1 \times 10^{-6}$  and  $5 \times 10^{-6}$   $\text{kg kg}^{-1}$  correspond to visibilities of approximately 4 km and 1 km, respectively. These two values will be subsequently used to track the height where the horizontally averaged liquid water mixing ratio is equal to these threshold values. Recall that fog is classified as such when the visibility falls below 1 km (NOAA 2017).

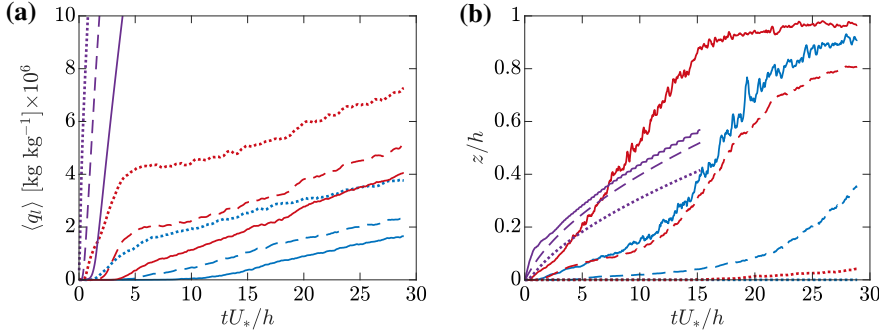


**Fig. 6** (a) Time series of the liquid water mixing ratio at different heights: dotted,  $z^+ \approx 0$ ; dashed,  $z^+ \approx 15$ ; solid,  $z/h \approx 0.1$ . (b) Time series of the height where  $\langle q_l \rangle$  is equal to a specified threshold,  $q_{l,t}$ : dotted,  $q_{l,t} = 5 \times 10^{-6}$ ; dashed,  $q_{l,t} = 1 \times 10^{-6}$ ; solid,  $q_{l,t} = 10^{-8}$  (saturation interface)  $\text{kg kg}^{-1}$ . Line colours denote cases: blue, 395M041 (weakly stable); red, 395M06 (weakly stable); purple, 395M205 (very stable)

A time series of the liquid water mixing ratio at different heights is shown in Fig. 6a, for both weakly stable cases (395M041 and 395M06) as well as a very stable case (395M205). For the weakly stable cases the flow nears laminarization in the first 5 eddy turnover times, which leads to the liquid water mixing ratio increasing rapidly. This is most obvious close to the ground for the case with the larger cooling rate, 395M06 (black dashed line, Fig. 6a). Thereafter,  $\langle q_l \rangle$  increases linearly with time for both cases and at all heights, although due to the larger cooling rate for case 395M06 the rate of increase of  $\langle q_l \rangle$  is larger than for case 395M041 (solid lines). In the very stable case (dotted lines), the reduced mixing of the laminar flow causes  $\langle q_l \rangle$  to increase significantly over a very short space of time, as well as at heights further from the ground. The liquid water mixing ratio reaches values of  $60 \times 10^{-6}$  and  $40 \times 10^{-6} \text{ kg kg}^{-1}$  at  $z/h \approx 0$  and  $z/h \approx 0.1$ , respectively, at time  $tU_* / h \approx 15$ , although this is not shown for clarity.

Figure 6b tracks the height where the horizontally averaged liquid water mixing ratio,  $\langle q_l \rangle$  is equal to a specified threshold, where we take the threshold values of  $q_{l,t} = 1 \times 10^{-6}$  and  $5 \times 10^{-6} \text{ kg kg}^{-1}$  mentioned above. Also shown is the interface between saturated and unsaturated air, obtained using a threshold of  $q_{l,t} = 10^{-8} \text{ kg kg}^{-1}$ . Note that choosing a different saturation interface threshold of, for example,  $q_{l,t} = 10^{-9} \text{ kg kg}^{-1}$  does not significantly alter the results presented in Fig. 6b as these are essentially all measures of the point where  $\langle q_v \rangle = q_{sat}$ . For the weakly stable cases the saturation interface rises rapidly from the ground and for case 395M06 it reaches the top of the domain ( $z/h = 1$ ) at around  $tU_* / h \approx 15$ . Due to the impermeability constraint with zero moisture flux, this top boundary would therefore now influence the development of liquid water. Indeed, we see the height based on  $q_{l,t} = 1 \times 10^{-6} \text{ kg kg}^{-1}$  ( $VIS \approx 4 \text{ km}$ , dark grey dashed line) increases rapidly at this point, as the turbulent mixing is now bringing already saturated air from aloft, rather than mixing unsaturated and saturated air as was previously the case. The flow after  $tU_* / h \approx 15$  for this case is therefore unlikely to be physical due to the influence of the top boundary. Nevertheless, at  $tU_* / h \approx 15$  the liquid water mixing ratio immediately adjacent to the ground is approximately  $5 \times 10^{-6} \text{ kg kg}^{-1}$ , corresponding to  $VIS \approx 1 \text{ km}$  and could thus be classified as fog. If a similar simulation were conducted of a turbulent Ekman layer then this would not be subject to the top boundary influence at  $tU_* / h \approx 15$ .

We would therefore expect the liquid water mixing ratio to continue to increase and as such show an increasingly larger region of fog.

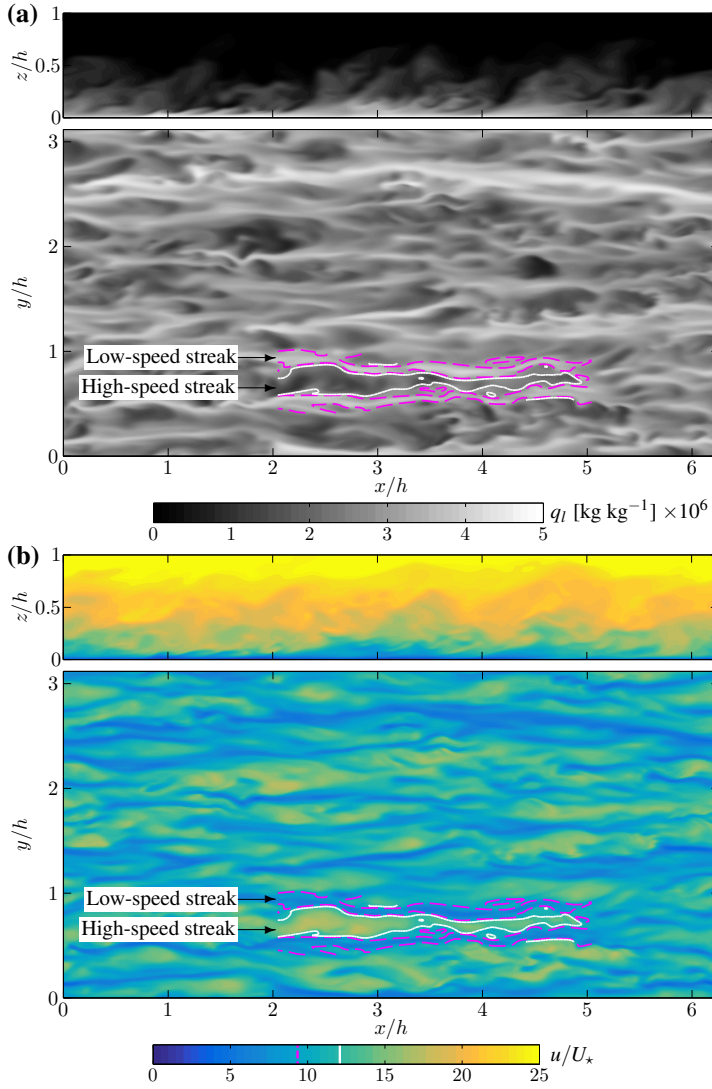
The very stable case, 395M205, shows that the visibility reduces significantly close to the ground. The saturation interface (light grey dotted line) grows at a similar rate compared to the weakly stable cases. Meanwhile, the height where  $\langle q_l \rangle$  is equal to either  $q_{l,t} = 1 \times 10^{-6}$  or  $5 \times 10^{-6} \text{ kg kg}^{-1}$  grows much more rapidly than the weakly stable cases. The latter threshold, along with Fig. 6a, suggests that large regions of the domain are filled with sheets of fog. This is due to the runaway cooling effect (Van de Wiel et al. 2007), wherein the lack of turbulent mixing causes the temperature to rapidly reduce and thus substantial condensation to occur. Here, the imposed ground cooling is approximately 3.4 times greater than the weakly stable case 395M06, yet the values of  $\langle q_l \rangle$  are over an order of magnitude larger.

Figure 7 shows an instantaneous snapshot of the liquid water mixing ratio and streamwise velocity at  $tU_* / h \approx 15$  for the turbulent case 395M06. This is the point at which almost the entirety of the air is at least somewhat saturated, indicating that further development of liquid water is unphysical due to the subsequent influence of the top boundary. The vertical cross-section of liquid water shows coherent structures that are inclined toward the horizontal, similar to the ‘ramp-like’ velocity structures observed in wall-bounded turbulence (Adrian et al. 2000; Marusic and Heuer 2007). The horizontal cross-section in a plane close to the ground at  $z^+ \approx 15$  shows that the liquid water and streamwise velocity contours are well correlated, where the highest liquid water content (or lowest visibilities) are associated with the streamwise-elongated streaks of low-speed streamwise velocity and conversely the low liquid water regions (higher visibility) are associated with high-speed streaks. These streaks (Kline et al. 1967) are accompanied by shorter quasi-streamwise vortices (Jeong et al. 1997). A snapshot showing isosurfaces of the streaks ( $u^+ - \langle u^+ \rangle = \pm 3$ ) and quasi-streamwise vortices ( $|w^+| = 2$ ) is given in Fig. 8a, where these isotach thresholds are taken from Jiménez (2018).

The streaks and quasi-streamwise vortices form the basis of the near-wall cycle, which is the well-documented self-sustaining mechanism that generates turbulence in the buffer region (Hamilton et al. 1995; Jiménez and Pinelli 1999; Schoppa and Hussain 2002; Jiménez 2018). A sketch is presented in Fig. 8b showing how this mechanism relates to fog. The quasi-streamwise vortices draw cooler air with reduced momentum away from ground in a process called an ejection. These form low-speed streaks and contain more liquid water. Meanwhile, the vortices also cause a downwash of warmer, drier air from aloft towards the ground. This process, termed a sweep, forms the high-speed streaks. The streaks meander perpendicular to the flow direction and eventually break down in a process called bursting, leading to vorticity generation and regeneration of the quasi-streamwise vortices. This therefore completes the self-sustaining cycle (Hwang and Bengana 2016; Jiménez 2018).

In the context of fog, the ejections enable the saturation interface (Fig. 6b) to grow quickly with time, as this mechanism rapidly draws liquid water away from the ground. However, the sweeps draw down drier air so that the horizontally averaged liquid water mixing ratio does not increase as rapidly as in the laminar case. This view is consistent with studies of particle-laden turbulent flows, where high concentrations of particles were observed to accumulate within low-speed streaks (e.g. Rashidi et al. 1990; Pan and Banerjee 1996; Soldati and Marchioli 2009; Lee and Lee 2015). Note that the higher Reynolds number cases with  $Re_* = 590$  include the same mechanism to that displayed in Fig. 8 (not shown). Furthermore, in neutrally stratified flows a similar set of self-sustaining streaky structures appear higher up in the boundary layer, albeit at larger length scales on the order of  $h$  and with bursting time scales of  $tu_\tau / h \sim 6$  (Flores and Jiménez 2010; Hwang 2015;





**Fig. 7** Instantaneous visualization of (a) liquid water mixing ratio and (b) streamwise velocity, in the streamwise–vertical  $(x-z)$  plane and horizontal  $(x-y)$  plane at  $z^+ \approx 15$ , for case 395M06 at  $tU_*/h \approx 15$ . Solid white and dashed magenta contours in lower-centre region of the horizontal planes (between  $2 \leq x/h \leq 5$ ) show  $\langle u \rangle \pm 0.5u'_{rms}$  to highlight a few high- and low-speed streaks. Mean flow is from left to right

Cossu and Hwang 2017; MacDonald et al. 2017). This suggests that the mechanism for fog formation shown in Fig. 8 is not limited to the near-ground region or to the low Reynolds numbers of the present simulations. We finally note that these streaky structures are somewhat reminiscent of the submeso motions that have been identified in SBL observational studies (Mahrt 2014). Under conditions of very weak shear with  $u_\tau \approx 0.02 \text{ m s}^{-1}$  and a surface layer height of  $h \approx 1 \text{ m}$  (Flores and Riley 2011) we would expect the bursting

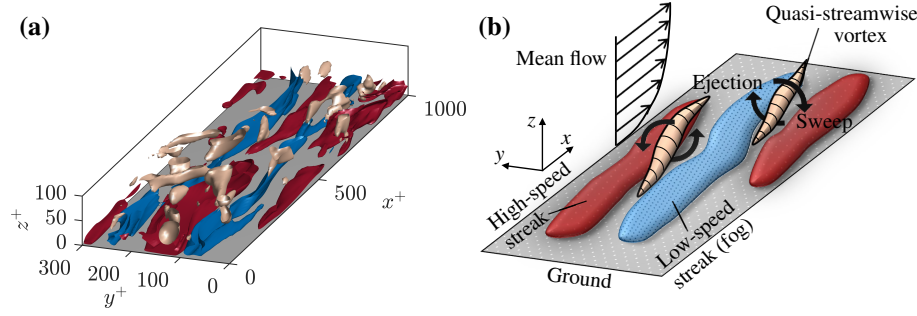


**Fig. 8** (a) Snapshot showing isosurfaces of high- and low-speed streaks ( $u^+ - \langle u^+ \rangle = \pm 3$ , red and blue respectively) and quasi-streamwise vortices ( $|w^+| = 2$ , tan). Structures above  $z^+ = 60$  are removed. (b) Sketch of the near-ground low- and high-speed streaks accompanied by quasi-streamwise vortices. Increased liquid water content (fog) concentrates in the low-speed streaks

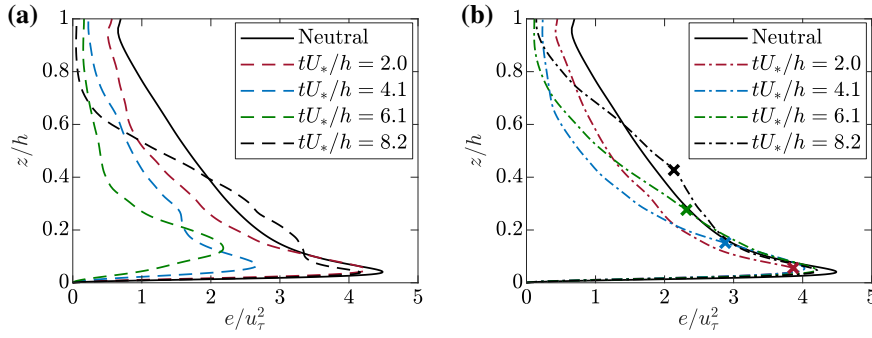


**Fig. 9** Profiles of TKE at different times during the initial fog formation stage, for (a) 395D06, and (b) 395M06. The solid black line represents the statistically steady dry neutrally stratified case. The  $\times$  symbols in (b) indicate the height of the saturation interface (Fig. 6b)

period to be of the order of several minutes, in agreement with the time scales associated with submeso (or at least hybrid) motions (Mahrt 2014).

### 3.3 Turbulence Collapse in Dry and Moist Flows

As discussed above, the weakly stable cases approach a laminar state before returning to be completely turbulent. In order to investigate this process, Fig. 9 shows the profiles of TKE at different times when liquid water first condenses. This is non-dimensionalized on the instantaneous friction velocity,  $u_\tau$ , at the corresponding times, as Flores and Riley (2018) shows the flow scales with instantaneous  $u_\tau$  close to the ground for weak stratification. Initially,  $e$  is close to the neutral case at  $tU_*/h = 2.0$  for both dry and moist cases. Thereafter, for the dry case, the TKE significantly reduces, with the peak value close to half of that of the neutral case. At  $tU_*/h = 8.2$ , the dry TKE has returned to a similar value of the neutral case, although there is very little energy above  $z/h \approx 0.8$ . Conversely, in the moist case (Fig. 9b), the TKE remains similar to the neutral case. There is some variation in the outer layer, although the peak value close to  $z/h \approx 0.04 \Rightarrow z^+ \approx 15$  consistently remains above  $e/u_\tau^2 \approx 4$ . Over this time period, the saturation interface grows from  $z/h \approx 0.05$  at

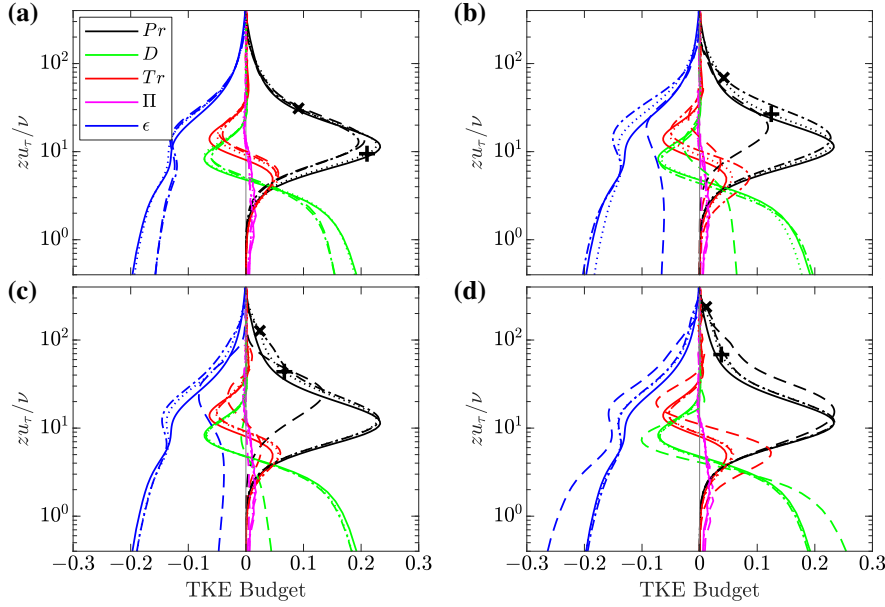


**Fig. 10** TKE budget for 395D00 (solid), 395M041 (dotted), 395D06 (dashed) and 395M06 (dash-dotted), at times (a)  $tU_*/h = 2.0$ , (b)  $tU_*/h = 4.1$ , (c)  $tU_*/h = 6.1$  and (d)  $tU_*/h = 8.2$ , as in Fig. 9. The budget terms are defined in Eq. 16 and are normalized on the instantaneous friction velocity,  $u_\tau$ , and viscosity,  $\nu$ . The black  $+$  and  $\times$  symbols indicate the height of the saturation interface (Fig. 6b) for 395M041 and 395M06, respectively. The buoyant production term,  $B$ , is small and not shown

$tU_*/h = 2$  to  $z/h \approx 0.41$  at  $tU_*/h = 8.2$  (shown by the  $\times$  symbols). The condensation of liquid water therefore appears to produce significant TKE, agreeing with the ‘burst’ of TKE observed in LES studies at the very onset of fog formation (Nakanishi 2000; Bergot 2013).

The TKE budget is shown in Fig. 10 for the same times as Fig. 9, where the budget terms are normalized on the instantaneous friction velocity,  $u_\tau$  and viscosity  $\nu$ . Note that due to the transient nature of these cooling cases and variations in TKE, the tendency or residual term is non-zero; however, it is typically of similar magnitude to the pressure correlation term, and thus is not shown for clarity. Similarly, the buoyant production of TKE,  $B$ , is small and not shown. The small magnitude of  $B$  has been discussed previously in DNS studies of stably stratified uniformly sheared flow (Jacobitz et al. 1997) and Ekman layers (Shah and Bou-Zeid 2014; Ansonge and Mellado 2014). There it has been suggested that the main influence of stable stratification on TKE is in reducing the vertical velocity variance, rather than directly through buoyant destruction of TKE.

Initially, at  $tU_*/h = 2.0$  (Fig. 10a), both the dry and moist TKE budget terms for  $h/L = 0.6$  (dashed and dash-dotted lines, respectively) are almost identical and in moderate agreement with the neutral case. However, at times  $tU_*/h = 4.1$  and  $6.1$  (Fig. 10b, c), the dry TKE production has significantly reduced compared to the neutral and moist cases. This reduction is somewhat balanced by a reduction in dissipation, as was also noted for the horizontal and vertical kinetic energies in Flores and Riley (2018). The formation of liquid water in the moist case, where the height of the saturation interface is shown by the  $\times$  symbols, appears to maintain the production of TKE similar to that of the neutral case.

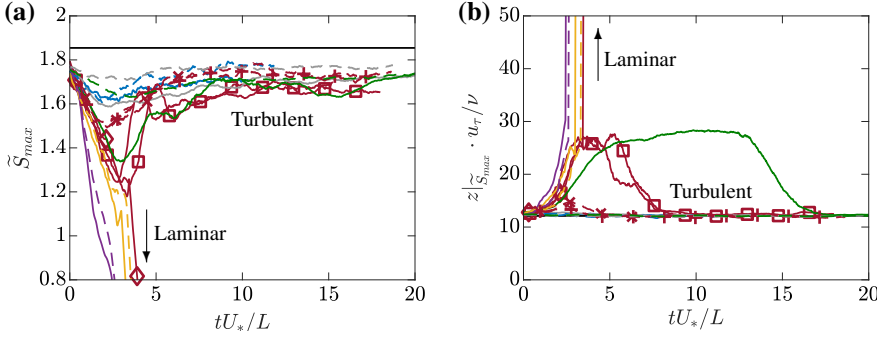


**Fig. 11** Time series of (a) the maximum non-dimensional shear rate  $\tilde{S}_{max} = \max((Pr+B)/\epsilon)$  and (b) the vertical position of this maximum, non-dimensionalized on the instantaneous friction velocity  $u_\tau$ . Line styles same as Fig. 3. The mean steady state values of dry neutral case 395D00 are given by the horizontal black lines. Data are only shown when  $Pr\nu/u_\tau^4 > 0.01$  (i.e., the flow is turbulent)

However, at  $z^+ \approx 15$  the dissipation of the moist case is always greater in magnitude when compared to the neutral case for all times. Even at  $tU_* / h = 8.2$ , when the dry and moist cases are returning to similar balances as the neutral case, the dissipation always remains somewhat larger than in the neutral case at this vertical location.

The moist case with a smaller cooling rate,  $h/L = 0.41$  (dotted lines, Fig. 10), is observed to maintain an instantaneous equilibrium and remain similar to the neutral case throughout, although there is enhanced dissipation close to  $zu_\tau/\nu \approx 15$ . There is also slightly larger production in the outer layer for this moderate cooling case, as observed by Nieuwstadt (2005) and Flores and Riley (2018). The dry case for  $h/L = 0.41$  is similar to the moist case and so is not shown in Fig. 10. The condensation of liquid water therefore only appears to have a significant impact during the transient adjustment to the cooling rate, when the flow is close to laminarization.

Finally, we investigate the effect of condensation of liquid water on the high- and low-speed streaks observed in Fig. 7. As mentioned earlier, these streaks are a fundamental mechanism in generating turbulence in the buffer layer. The ratio between the instantaneous, horizontally averaged production and dissipation of TKE,  $\tilde{S}(z, t) = (Pr + B)/\epsilon$ , or non-dimensional local shear rate, was found to be related to the existence of streaks in Lam and Banerjee (1992). When  $\tilde{S} < 1$  and dissipation exceeds production, the low-speed streaks were no longer observed. Conversely, when production increases and  $\tilde{S} \gtrsim 1$  the streaks were found to be increasingly energetic and persistent with increasing  $\tilde{S}$ .

Figure 11a shows the evolution of the maximum of  $\tilde{S}$ , where data are only shown when the maximum production  $Pr\nu/u_\tau^4 > 0.01$ , or 5% of the maximum production in the dry neutrally stratified case. This is done because  $Pr$  and  $\epsilon$  tend to zero in the cases where turbulence collapses, making  $\tilde{S}$  undefined. Before turbulence collapses, in the laminar cases we see that  $\tilde{S}$  tends to below the critical value  $\tilde{S} \approx 1$ . The streaks therefore cannot remain self-sustaining and the near-wall cycle is destroyed. In the cases that remain turbulent,  $\tilde{S}$  initially reduces as the flow adjusts to the imposed cooling, before tending towards a steady state value that is nearly 10% less than the mean of the dry neutrally stratified case. This is due to enhanced dissipation in the cooling cases, as observed from the TKE budgets (Fig. 10). For moderate cooling rates of  $h/L = 0.41$ , little difference is seen between the dry and moist cases. However, for the weakly stable cases with stronger cooling of

$h/L = 0.6$  for both  $Re_* = 395$  and  $590$ ,  $\tilde{S}$  is slightly less for the dry case than for the moist case. This suggests that the condensation of liquid water energizes the near-wall cycle, promoting streaks and thus offering a possible explanation for how the flow is able to sustain turbulent motions at higher cooling rates than the dry case. From the TKE budgets in Fig. 10, this appears to be due to reduced dissipation in the moist case compared to the dry case, rather than increased TKE production. Neutrally stratified turbulent flows laden with heavy particles have also been seen to energize turbulent flows, although only for low Stokes number particles (Lee and Lee 2015). There, the mechanism is slightly different as the inertia of the particles imparts momentum on the fluid and increases TKE production, rather than reduced dissipation observed in the moist cases in this study.

Figure 11b shows the vertical position of the maximum local shear rate,  $z|_{\tilde{s}_{max}}$ , non-dimensionalized on the instantaneous friction velocity  $u_\tau$ . This indicates the position where streak formation is dominant; for the present dry neutral case this is located at approximately  $z^+ \approx 12$ , in agreement with Lam and Banerjee (1992). The weakly stable cases also show that the streak formation remains located at approximately  $zu_\tau/\nu \approx 12$ . For the very stable cases, the vertical position where streak formation is strongest is progressively pushed away from the ground, presumably until the reduced shear higher up cannot sustain streak generation and the turbulence collapses.

#### 4 Conclusions

The effects of moisture on the stably stratified surface layer are investigated using direct numerical simulations (DNS), with particular attention given to how this system can be treated as an idealized representation of fog formation. A cooling heat flux is imposed at the ground yielding both weakly stable (turbulent) and very stable (laminar) solutions, when initialized from a neutrally stratified turbulent surface layer. The relative humidity is initialized close to 100%, so that as the air cools it reaches its saturation point and liquid water condenses. In the weakly stable moist cases, the vertical height of the saturation interface grows quickly until it reaches the top of the domain. However, due to turbulent mixing the liquid water mixing ratio remains relatively small throughout the domain, with only the lowermost few percent of the surface layer achieving enough liquid water to correspond to visibilities close to 1 km. In the very stable cases the liquid water mixing ratio increases rapidly. While the saturation interface grows at a similar rate to the turbulent cases, the visibility significantly reduces below 1 km due to runaway cooling. This idealized system suggests that while turbulence and its associated mixing does not inhibit fog formation, it does impede its growth.

In the case where the ground cooling is close to its critical value ( $h/L \approx 0.6$  for  $Re_* = hU_*/\nu = 395$ ), two dry cases with unique initialization snapshots were found to sustain turbulent motions, while in another case with a different initialization snapshot it did not. Meanwhile, when moisture effects were enabled, the flow was able to sustain turbulent motions when initialized from the same three snapshots. Thus, for the moist case the critical cooling value is between  $0.6 < h/L < 0.7$  while for the dry case it was at most  $h/L \lesssim 0.6$  for  $Re_* = 395$ . The moist cases were not as close to laminarization, with the inner-normalized local Obukhov length  $L_\tau u_\tau/\nu$  always exceeding a value 225, while turbulence collapsed in the dry cases when  $L_\tau u_\tau \nu \lesssim 100$  (Flores and Riley 2011). The latent heat release through condensation appears to enhance TKE relative to the dry case, enabling the moist cases to sustain slightly larger ground cooling fluxes (or higher Richardson numbers) before leading to turbulence collapse. We hypothesize that any tendency towards laminarization with reduced mixing would result in enhanced cooling and

thus lead to condensation, producing additional mixing that would avert, or at least delay, complete turbulent collapse.

Visualization of the weakly stable moist cases reveal that regions of increased liquid water mixing ratio develop within the low-speed streaks associated with the well-documented near-wall cycle. These low-shear regions draw slower-moving air up from closer to the ground, and suggest a mechanism for how fog can form within turbulent flow. In neutrally stratified flows these streaky structures have also been observed at higher Reynolds number as well as at larger scales higher up in the boundary layer (Flores and Jiménez 2010; Hwang 2015; Cossu and Hwang 2017), and are somewhat reminiscent of the submeso motions in SBL observations (Mahrt 2014). This suggests that the mechanism for fog formation discussed in this paper, obtained from simulations of an idealized system at relatively modest Reynolds numbers, should also apply to the real atmosphere.

While the streaks of both dry and moist weakly stable cases are slightly weaker than in the neutrally stratified case, the moist case appears to produce streaks which are slightly more persistent and energetic than in the dry case. This is due to the dissipation of TKE being greater in the dry case than the moist case, although both are larger than in the neutral case. The shear production of TKE for the moist case appears to remain somewhat similar to the neutrally stratified case, although when saturation first occurs it results in a slight increase in production relative to the neutral case.

**Acknowledgements** This research was carried out at the Jet Propulsion Laboratory, California Institute of Technology, under a contract with the National Aeronautics and Space Administration. Parts of this research were supported by the U.S. Department of Energy, Office of Biological and Environmental Research, Earth System Modeling; the NASA MAP Program; the Office of Naval Research, Marine Meteorology Program and the NOAA/CPO MAPP Program. We thank the three anonymous reviewers for their constructive comments on the manuscript. The authors also acknowledge the Texas Advanced Computing Center (TACC) at The University of Texas at Austin for providing HPC resources that have contributed to the research results reported within this paper.

## Appendix 1: Effect of Computational Domain Size

In the present study, the domain size in the streamwise and spanwise directions is  $2\pi h \times \pi h$ , which is standard for neutrally stratified dry simulations (Lozano-Durán and Jiménez 2014; Munters et al. 2016). However, there can exist patches of laminar and turbulent flow in stably stratified flows close to laminarization, which are of size  $10h$  (that is, the present domain size). A small computational domain can therefore result in turbulent structures that get ‘locked’ in place due to the periodic boundary conditions (Flores and Riley 2011; García-Villalba and del Álamo 2011). This can require substantial time for the turbulence to repopulate the domain and does not represent a physically realistic scenario.

We double the domain size to  $4\pi h \times 2\pi h$  in the streamwise and spanwise directions, with the results shown in Fig. 12 for cooling with  $h/L = 0.6$  and  $Re_* = 395$ . We see a similar behaviour for both dry (solid) and moist (dashed) cases compared to the regular domain size. The peak around  $tU_*/h \approx 10$  for the dry case temperature fluctuations (Fig. 12b) is due to the turbulence becoming locked in place. Visual inspection of the velocity field of the dry case (not shown) reveals a similar pattern to Fig. 5 of Flores and Riley (2011), in which there exist stripes of turbulent and laminar flow extending down the entire streamwise length of the domain. The present larger domain dry case also exhibits this effect, where García-Villalba and del Álamo (2011) notes domains of at least  $8\pi h \times 3\pi h$  are required to observe

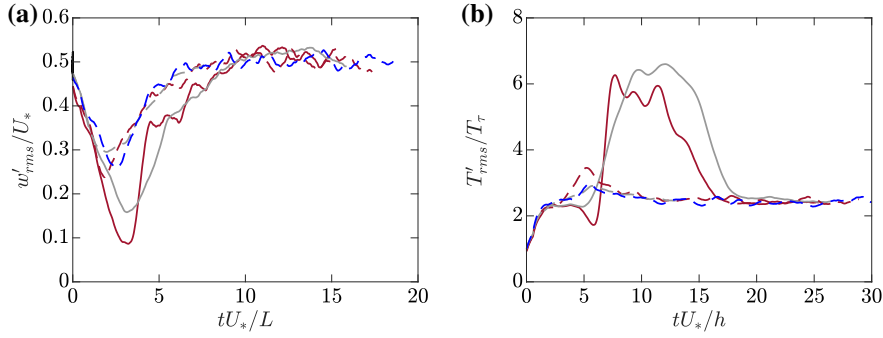


**Fig. 12** Time series of (a) r.m.s. vertical velocity fluctuations and (b) temperature fluctuations at  $z^+ = 15$ . Line styles are: red,  $h/L = 0.6$  with  $T_0 = 279$  K (base case); grey, base case except with enlarged domain; blue, base case except with  $T_0 = 285$  K. Solid lines denote dry cases, dashed denote moist cases

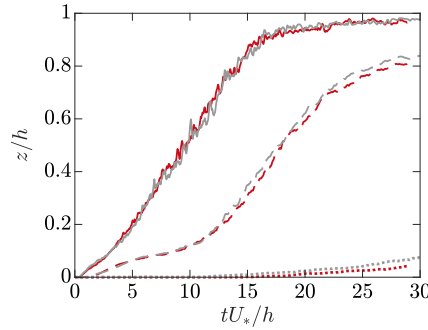


**Fig. 13** Same as Fig. 6b, showing time series of the height where  $\langle q_l \rangle$  is equal to a specified threshold,  $q_{l,t}$ : dotted,  $q_{l,t} = 5 \times 10^{-6}$ ; dashed,  $q_{l,t} = 1 \times 10^{-6}$ ; and solid,  $q_{l,t} = 10^{-8}$  (saturation interface)  $\text{kg kg}^{-1}$ , for the weakly stable case 395M06 with  $h/L = 0.6$ . Line colours: red,  $T_0 = 279$  K (base case); grey,  $T_0 = 285$  K

intermittency in the streamwise direction for statistically steady flows. This behaviour is not observed in any of the moist case, as presumably the mixing induced by condensation is sufficient to completely avoid these large laminar patches at these cooling rates. In this work, as in Flores and Riley (2011), we ignore data from when the turbulent flow is locked in place, as it is artificial. This is primarily of concern for the dry cases, and was not observed for the moist cases.

## Appendix 2: Effect of Initial Temperature

Given that the liquid water mixing ratio depends non-linearly on temperature, we also investigate the effect of the temperature at which the simulations are initialized,  $T_0$ . For the cases studied in this paper, we set  $T_0 = 279.15$  K, while here we increase the initial temperature to 285.15 K, for matched cooling rates of  $h/L = 0.6$ . Figure 13 shows the time series of fog height, as in Fig. 6b for these two initial temperatures. The two cases are initially similar although they start to diverge after approximately  $tU_*/h \gtrsim 15$ , at which point the interface

between saturated and unsaturated water has reached the top boundary. The vertical velocity and temperature fluctuations shown in Fig. 12 also show good agreement between the base case (red dashed line) and increased initial temperature case (blue dashed line). This suggests that, while the temperature will be important for specific meteorological events, it is likely not relevant here given the idealized system studied in this paper.

## References

- Adrian RJ, Meinhart CD, Tomkins CD (2000) Vortex organization in the outer region of the turbulent boundary layer. *J Fluid Mech* 422:1–54
- Andrejczuk M, Grabowski WW, Malinowski SP, Smolarkiewicz PK (2004) Numerical simulation of cloud–clear air interfacial mixing. *J Atmos Sci* 61:1726–1739
- Andrejczuk M, Grabowski WW, Malinowski SP, Smolarkiewicz PK (2006) Numerical simulation of cloud–clear air interfacial mixing: Effects on cloud microphysics. *J Atmos Sci* 63:3204–3225
- Andrejczuk M, Grabowski WW, Malinowski SP, Smolarkiewicz PK (2009) Numerical simulation of cloud–clear air interfacial mixing: Homogeneous versus inhomogeneous mixing. *J Atmos Sci* 66:2493–2500
- Ansorge C, Mellado JP (2014) Global intermittency and collapsing turbulence in the stratified planetary boundary layer. *Boundary-Layer Meteorol* 153:89–116
- Barkstrom BR (1978) Some effects of 8–12  $\mu\text{m}$  radiant energy transfer on the mass and heat budgets of cloud droplets. *J Atmos Sci* 35:665–673
- Bergot T (2013) Small-scale structure of radiation fog: a large-eddy simulation study. *Q J R Meteorol Soc* 139:1099–1112
- Bergot T (2016) Large-eddy simulation study of the dissipation of radiation fog. *Q J R Meteorol Soc* 142:1029–1040
- Bott A, Sievers U, Zdunkowski W (1990) A radiation fog model with a detailed treatment of the interaction between radiative transfer and fog microphysics. *J Atmos Sci* 47:2153–2166
- Bou-Zeid E, Higgins C, Huwald H, Meneveau C, Parlange MB (2010) Field study of the dynamics and modelling of subgrid-scale turbulence in a stable atmospheric surface layer over a glacier. *J Fluid Mech* 665:480–515
- Brown R, Roach WT (1976) The physics of radiation fog: II—a numerical study. *Q J R Meteorol Soc* 102:335–354
- Businger JA (1982) The fluxes of specific enthalpy, sensible heat and latent heat near the Earth’s surface. *J Atmos Sci* 39:1889–1892
- Chung D, Matheou G (2014) Large-eddy simulation of stratified turbulence. Part I: A vortex-based subgrid-scale model. *J Atmos Sci* 71:1863–1879
- Cossu C, Hwang Y (2017) Self-sustaining processes at all scales in wall-bounded turbulent shear flows. *Phil Trans R Soc A* 375:20160,088
- Deardorff JW (1980) Stratocumulus-capped mixed layers derived from a three-dimensional model. *Boundary-Layer Meteorol* 18:495–527
- Duynkerke PG (1999) Turbulence, radiation and fog in Dutch stable boundary layers. *Boundary-Layer Meteorol* 90:447–477
- Elliott WP (1958) The growth of the atmospheric internal boundary layer. *Trans Am Geophys Union* 39:1048–1054
- Flores O, Jiménez J (2010) Hierarchy of minimal flow units in the logarithmic layer. *Phys Fluids* 22:071,704



- Flores O, Riley JJ (2011) Analysis of turbulence collapse in the stably stratified surface layer using direct numerical simulation. *Boundary-Layer Meteorol* 139:241–259
- Flores O, Riley JJ (2018) Energy balance in stably-stratified, wall-bounded turbulence. In: Clercx HJH, van Heijst GJF (eds) *Mixing and Dispersion in Flows Dominated by Rotation and Buoyancy*, Springer, pp 89–99
- Gage KS, Reid WH (1968) The stability of thermally stratified plane Poiseuille flow. *J Fluid Mech* 33:21–32
- García-Villalba M, del Álamo JC (2011) Turbulence modification by stable stratification in channel flow. *Phys Fluids* 23:045.104
- Gohari SMI, Sarkar S (2017) Direct numerical simulation of turbulence collapse and rebirth in stably stratified Ekman flow. *Boundary-Layer Meteorol* 162:401–426
- Grabowski WW, Smolarkiewicz PK (1990) Monotone finite-difference approximations to the advection-condensation problem. *Mon Weather Rev* 118:2082–2098
- Grabowski WW, Smolarkiewicz PK (2002) A multiscale anelastic model for meteorological research. *Mon Weather Rev* 130:939–956
- Gultepe I, Tardif R, Michaelides SC, Cermak J, Bott A, Bendix J, Müller MD, Pagowski M, Hansen B, Ellrod G, Jacobs W, Toth G, Cober SG (2007) Fog research: A review of past achievements and future perspectives. *Pure Appl Geophys* 164:1121–1159
- Hamilton JM, Kim J, Waleffe F (1995) Regeneration mechanisms of near-wall turbulence structures. *J Fluid Mech* 287:317–348
- Hwang Y (2015) Statistical structure of self-sustaining attached eddies in turbulent channel flow. *J Fluid Mech* 767:254–289
- Hwang Y, Bengana Y (2016) Self-sustaining process of minimal attached eddies in turbulent channel flow. *J Fluid Mech* 795:708–738
- Izett JG, Schilperoort B, Coenders AMJ, Baas P, Bosveld FC, van de Wiel BJH (2019) Missed fog?: On the potential of obtaining observations at increased resolution during shallow fog events. *Boundary-Layer Meteorol* DOI 10.1007/s10546-019-00462-3
- Jacobitz FG, Sarkar S, Van Atta CW (1997) Direct numerical simulations of the turbulence evolution in a uniformly sheared and stably stratified flow. *J Fluid Mech* 342:231–261
- Jeong J, Hussain F, Schoppa W, Kim J (1997) Coherent structures near the wall in a turbulent channel flow. *J Fluid Mech* 332:185–214
- Jiménez J (2018) Coherent structures in wall-bounded turbulence. *J Fluid Mech* 842:P1
- Jiménez J, Pinelli A (1999) The autonomous cycle of near-wall turbulence. *J Fluid Mech* 389:335–359
- Kim J, Moin P, Moser R (1987) Turbulence statistics in fully developed channel flow at low Reynolds number. *J Fluid Mech* 177:133–166
- Kline SJ, Reynolds WC, Schraub FA, Runstadler PW (1967) The structure of turbulent boundary layers. *J Fluid Mech* 30:741–773
- Kozul M, Chung D, Monty JP (2016) Direct numerical simulation of the incompressible temporally developing turbulent boundary layer. *J Fluid Mech* 796:437–472
- Kunkel BA (1984) Parameterization of droplet terminal velocity and extinction coefficient in fog models. *J Clim Appl Meteorol* 23:34–41
- Kurowski MJ, Grabowski WW, Smolarkiewicz PK (2014) Anelastic and compressible simulation of moist deep convection. *J Atmos Sci* 71:3767–3787
- Lam K, Banerjee S (1992) On the condition of streak formation in a bounded turbulent flow. *Phys Fluids* 4:306–320
- Lee J, Lee C (2015) Modification of particle-laden near-wall turbulence: Effect of Stokes number. *Phys Fluids* 27:023,303
- Lilly DK (1962) On the numerical simulation of buoyant convection. *Tellus* 14:148–172

- Lozano-Durán A, Jiménez J (2014) Effect of the computational domain on direct simulations of turbulent channels up to  $Re_\tau = 4200$ . *Phys Fluids* 26:011,702
- de Lozar A, Mellado JP (2015) Mixing driven by radiative and evaporative cooling at the stratocumulus top. *J Atmos Sci* 72:4681–4700
- de Lozar A, Mellado JP (2017) Reduction of the entrainment velocity by cloud droplet sedimentation in stratocumulus. *J Atmos Sci* 74:751–765
- MacDonald M, Chung D, Hutchins N, Chan L, Ooi A, García-Mayoral R (2017) The minimal-span channel for rough-wall turbulent flows. *J Fluid Mech* 816:5–42
- Mahrt L (1999) Stratified atmospheric boundary layers. *Boundary-Layer Meteorol* 90:375–396
- Mahrt L (2014) Stably stratified atmospheric boundary layers. *Annu Rev Fluid Mech* 46:23–45
- Maronga B, Bosveld FC (2017) Key parameters for the life cycle of nocturnal radiation fog: a comprehensive large-eddy simulation study. *Q J R Meteorol Soc* 143:2463–2480
- Marusic I, Heuer WDC (2007) Reynolds number invariance of the structure inclination angle in wall turbulence. *Phys Rev Lett* 99:114,504
- Mazoyer M, Lac C, Thouron O, Bergot T, Massonv V, Musson-Genon L (2017) Large eddy simulation of radiation fog: impact of dynamics on the fog life cycle. *Atmos Chem Phys* 17:13,017–13,035
- Mellado JP (2010) The evaporatively driven cloud-top mixing layer. *J Fluid Mech* 660:5–36
- Mellado JP (2012) Direct numerical simulation of free convection over a heated plate. *J Fluid Mech* 712:418–450
- Mellado JP, Stevens B, Schmidt H, Peters N (2010) Two-fluid formulation of the cloud-top mixing layer for direct numerical simulation. *Theor Comput Fluid Dyn* 24:511–536
- Mellado JP, Stevens B, Schmidt H (2014) Wind shear and buoyancy reversal at the top of stratocumulus. *J Atmos Sci* 71:1040–1057
- Moeng CH (1984) A large-eddy-simulation model for the study of planetary boundary-layer turbulence. *J Atmos Sci* 41:2052–2062
- Moin P, Kim J (1982) Numerical investigation of turbulent channel flow. *J Fluid Mech* 118:341–377
- Moin P, Mahesh K (1998) Direct numerical simulation: a tool in turbulence research. *Annu Rev Fluid Mech* 30(1):539–578
- Monin AS (1970) The atmospheric boundary layer. *Annu Rev Fluid Mech* 2:225–250
- Moser RD, Kim J, Mansour NN (1999) Direct numerical simulation of turbulent channel flow up to  $Re_\tau = 590$ . *Phys Fluids* 11:943–945
- Munters W, Meneveau C, Meyers J (2016) Shifted periodic boundary conditions for simulations of wall-bounded turbulent flows. *Phys Fluids* 28:025,112
- Nakanishi M (2000) Large-eddy simulation of radiation fog. *Boundary-Layer Meteorol* 94:461–493
- Nieuwstadt FTM (2005) Direct numerical simulation of stable channel flow at large stability. *Boundary-Layer Meteorol* 116:277–299
- NOAA (2017) Federal Meteorological Handbook No. 1, Surface Weather Observations and Reports. US Department of Commerce/NOAA, Tech Rep FCM-H1-2017
- Oliver DA, Lewellen WS, Williamson GG (1978) The interaction between turbulent and radiative transport in the development of fog and low-level stratus. *J Atmos Sci* 35:301–316
- Pan Y, Banerjee S (1996) Numerical simulation of particle interactions with wall turbulence. *Phys Fluids* 8:2733–2755

- Panofsky HA, Townsend AA (1964) Change of terrain roughness and the wind profile. *Q J R Meteorol Soc* 90:147–155
- Porson A, Price J, Lock A, Clark P (2011) Radiation fog. Part II: Large-eddy simulations in very stable conditions. *Boundary-Layer Meteorol* 139:193–224
- Price J (2011) Radiation fog. Part I: Observations of stability and drop size distributions. *Boundary-Layer Meteorol* 139:167–191
- Price JD, Clark R (2014) On the measurement of dewfall and fog-droplet deposition. *Boundary-Layer Meteorol* 152:367–393
- Prusa JM, Smolarkiewicz PK, Wyszogrodzki AA (2008) EULAG, a computational model for multiscale flows. *Comput Fluids* 37:1193–1207
- Rashidi M, Hetsroni G, Banerjee S (1990) Particle-turbulence interaction in a boundary layer. *Int J Multiph Flow* 16:935–949
- Roach WT (1976) On the effect of radiative exchange on the growth by condensation of a cloud or fog droplet. *Q J R Meteorol Soc* 102:361–372
- Roach WT, Brown R, Caughey SJ, Garland JA, Readings CJ (1976) The physics of radiation fog: I—a field study. *Q J R Meteorol Soc* 102:313–333
- Rodhe B (1962) The effect of turbulence on fog formation. *Tellus* 14:49–86
- de Rooze SR, Jonker HJJ, van de Wiel BJH, Vertregt V, Perrin V (2017) A diagnosis of excessive mixing in Smagorinsky subfilter-scale turbulent kinetic energy models. *J Atmos Sci* 74:1495–1511
- Schoppa W, Hussain F (2002) Coherent structure generation in near-wall turbulence. *J Fluid Mech* 453:57–108
- Shah SK, Bou-Zeid E (2014) Direct numerical simulations of turbulent Ekman layers with increasing static stability: modifications to the bulk structure and second-order statistics. *J Fluid Mech* 760:494–539
- Smolarkiewicz PK, Margolin LG (1997) On forward-in-time differencing for fluids: An Eulerian/semi-Lagrangian non-hydrostatic model for stratified flows. *Atmos-Ocean* 35:127–152
- Smolarkiewicz PK, Margolin LG (1998) MPDATA: A finite-difference solver for geophysical flows. *J Comput Phys* 140:459–480
- Soldati A, Marchioli C (2009) Physics and modelling of turbulent particle deposition and entrainment: Review of a systematic study. *Int J Multiph Flow* 35:827–839
- Steenefeld GJ, Ronda RJ, Holtslag AAM (2015) The challenge of forecasting the onset and development of radiation fog using mesoscale atmospheric models. *Boundary-Layer Meteorol* 154:265–289
- Stull RB (1988) *An Introduction to Boundary Layer Meteorology*. Kluwer Academic Publishers
- Taylor GI (1917) The formation of fog and mist. *Q J R Meteorol Soc* 43:241–268
- Teixeira J (1999) Simulation of fog with the ECMWF prognostic cloud scheme. *Q J R Meteorol Soc* 125:529–552
- Welch RM, R MG, Cox SK (1986) Prediction of quasi-periodic oscillations in radiation fogs. Part I: Comparison of simple similarity approaches. *J Atmos Sci* 43:633–651
- Van de Wiel BJH, Moene AF, Steeneveld GJ, Hartogensis OK, Holtslag AAM (2007) Predicting the collapse of turbulence in stably stratified boundary layers. *Flow Turbul Combust* 79:251–274